

M83. I. MULTICOLOR SURFACE PHOTOMETRY

RAYMOND J. TALBOT, JR.,* ERIC B. JENSEN,† AND REGINALD J. DUFOUR*

Rice University

Received 1978 July 14; accepted 1978 October 4

ABSTRACT

UBVR surface photometry of the bright southern spiral galaxy NGC 5236 (M83) is presented, based on CTIO 4 m prime focus plates and photoelectric photometry obtained at CTIO and KPNO. Maps of the galaxy in $B - V$, $U - B$, and the "reddening-free" parameter $Q = (U - B) - 0.72(B - V)$ are presented and analyzed. Radial profiles of the brightness and colors are discussed.

We have used color and morphological information to correct the radial surface brightness profile for the effects of recent ($t < 10^8$ years) star formation; by doing so, we have removed the "hump" in the profile characteristic of Freeman's Type II profiles, leaving a profile indistinguishable from his Type I, although M83 was his prototype for Type II.

We have used the Q map to search for color gradients across and behind arms. If the star formation regions drift through the material, as predicted by the density-wave theory, the colors should become systematically redder downstream from the shock wave. We have found no quantitative evidence for drift in the color maps either in the vicinity of the bright arms or in the smooth red regions between them. However, these results turn out to be consistent with a careful interpretation of the theory when one allows for noncircular orbits of newly formed stars and for imperfect synchrony of star formation.

Our *UBVR H α* intensity maps are available on computer tape, upon request, from the first author.

Subject headings: galaxies: individual — galaxies: photometry — galaxies: structure

I. INTRODUCTION

a) *The General Problem*

Two of the most fundamental properties of galaxies that remain poorly understood are the nature of the spiral structure that dominates many galaxies and the nature of the processes that drive the vigorous star formation which is still occurring in many of their nuclei and which is particularly prominent in their spiral arms. We believe that considerable progress has been made in the past 15 years toward understanding the nature of both the spiral structure and the star-forming mechanisms, due to the introduction of the density wave theory of Lin and Shu (1964). In the density wave theory, the observed spiral structure is taken to be some combination of observable manifestations of a self-propagating wavelike density perturbation in the basically axisymmetrically distributed material that makes up the disk of the galaxy; the spiral shape occurs through the way the density perturbation propagates in a differentially rotating system. Furthermore, Fujimoto (1968) and Roberts (1969) have shown that in the presence of a density

wave of moderate amplitude, shock waves are likely to be produced in the interstellar medium in the vicinity of the minima of the spiral gravitational potential. It is then appealing to explain the strikingly long, well-organized spiral dust lanes that are among the most prominent features of many spirals as the visible manifestations of this shock, and to ascribe the vigorous star formation that occurs on one side of the dust lanes to the effect of the shock on already formed clouds that have recently passed through it (Woodward 1976).

Despite considerable theoretical work in the 15 years since the introduction of the density wave theory, this theory might still be better termed an hypothesis, since no one has yet managed even to show conclusively that such a gravitationally propagating density disturbance can exist in a real galaxy, and, if it does exist, what the mechanisms are that cause its generation, maintenance, and decay; we refer the reader to Toomre (1977) for a discussion of the current status of the density wave theory. It is rather in observational work where the density wave theory has perhaps made its most concrete contribution, since it remains the only explanation of spiral structure that has been worked out in enough detail to be amenable to observational test. In particular, it should at least be possible to establish observationally whether the spiral structure is the manifestation of a wave phenomenon that is propagating *through* the material in the disk of a spiral galaxy. We consider the primary

* Visiting Astronomer, Cerro Tololo Inter-American Observatory, operated by the Association of Universities for Research in Astronomy, Inc., under contract with the National Science Foundation.

† Visiting Astronomer, Kitt Peak National Observatory, operated by the Association of Universities for Research in Astronomy, Inc., under contract with the National Science Foundation.

observational evidence that currently bears on this problem to be as follows:

1. The existence of the frequently occurring sequence dust lane → H II regions → blue associations was discussed extensively by Lynds (1970, 1972, 1974), with the dust lanes invariably occurring on the inside of the arms, or at least interior to the H II regions in those galaxies where many of the H II regions lie like beads on a string along the spiral arms. We shall show that the inner parts of M83 provide a particularly striking example of this phenomenon; other excellent examples from Lynds's (1974) catalog include M51, M100, and NGC 157. However, in other galaxies such as NGC 2403, star formation is occurring in the vicinity of the arms without any evidence for the existence of "grand design" dust lanes. We shall also show that the outer parts of M83 show considerably less organization than the inner parts; hence, within a single galaxy, the physical conditions governing the nature of the spiral structure vary.

2. The work of Rots at Westerbork (1975; see also Visser 1978), mapping the velocity field of M81 at 21 cm, shows velocity fluctuations in the vicinity of the spiral arms in exactly the manner and with the amplitude expected from the density wave picture. Furthermore, a density wave model constructed by Rots in the same work and compared to *BV* surface photometry of the galaxy shows a displacement between the bluest part of the arms and the density wave crest, the displacement amounting to about 10–20 million years drift in the density wave picture. Again, this seems just what would be expected if the star formation in the arms of M81 were induced by the action of a shock on previously formed dense clouds.

3. Broad spiral patterns appear to exist in the surface mass density distributions in spiral galaxies, detected as positional fluctuations in the light of the old stellar component in the disks of these galaxies. Evidence for these broad spiral patterns, correctly interpreted, was first presented by Schweizer (1976) and has subsequently been corroborated by Jensen (1977) from surface photometry at wavelengths as long as 1 μm . In the density wave picture, these broad spiral patterns can be interpreted to be the density waves themselves.

For a thorough discussion of observational tests of the density wave theory prior to our work, we refer the reader to Schweizer (1975).

b) Present Work

We have obtained and analyzed surface photometry of the bright southern spiral galaxy NGC 5236 (M83), revised Hubble type SAB(s)c, luminosity class I-II (de Vaucouleurs, de Vaucouleurs, and Corwin 1976, hereafter RC2). Our work differs from earlier work by Schweizer (1976) in that we have obtained calibrated surface photometry in the standard Johnson passbands *U*, *B*, *V*, and *R* (as well as in other passbands), rather than in passbands defined primarily by observational convenience. We have thus been able to compare the color maps we have produced (*U* – *B*, *B* – *V*, etc.)

with models of evolving mixes of stellar populations, in the manner pioneered by Dixon, Ford, and Robertson (1972) and Searle, Sargent, and Bagnuolo (1973). Our work, like Schweizer's, has been largely motivated by the desire to establish a measurable *drift velocity* of the young associations supposedly formed in the wake of the spiral density wave, relative to some feature such as the dust lane which supposedly is "anchored" to the density wave. However, by our use of models, not only for the aging and mixing of the stellar light but also for the interstellar extinction in M83, we can make much more stringent (albeit model-dependent) tests for drift than have been previously possible, even allowing for the varying contribution of the light from the disk of old stars underlying the arms. In addition, we can make detailed estimates of the amount and location of star formation that is occurring over the face of M83, and the amount and distribution of the dust causing the extinction within this galaxy. In §§ II and III, we present our observations, reduction methods, and the luminosity and color maps; in § IV, we discuss radial and azimuthal profiles of the luminosity and colors; in § V, we investigate whether there is evidence for the hypothesis that the spiral structure propagates through the material of the galaxy; and in § VI, we summarize our conclusions and prospects for future work.

II. OBSERVATIONAL MATERIALS AND REDUCTION TECHNIQUES

a) Calibrated Photography

Prime focus plates were obtained with the CTIO 4 m telescope during 1976 June by two of the authors (R. J. T. and R. J. D.). Table 1 lists the emulsion and filter combinations used, together with the exposure time, date of acquisition, and seeing and air mass conditions for each plate. All plates were taken with identical camera positions, guide box coordinates, and guide star. The emulsion and filter combinations were chosen to match closely the standard Johnson *UBVR* photoelectric passbands. This choice has allowed us readily to compare our photometric results to the large number of photoelectric data available on individual stars and integrated light of clusters and associations. Multiple plates with widely varying exposure times were obtained, covering a wide range of intensity while simultaneously permitting the reduction of statistical errors over most of the range by combining data from two or three plates. All of the plates were obtained under estimated seeing conditions of $\lesssim 2''.5$.

All calibrations were exposed simultaneously with the galaxy photographs with the 16 spot Inconel step wedge sensitometer (No. 117) built into the CTIO prime focus camera. Generally, six to 12 spots provided calibrations for photographic densities ranging from the fog level to $D = 4.0$. The plates were developed, fixed, and washed for the same time intervals and with the same temperature and nitrogen-burst agitation (4 minutes, *D*-19, 20°C). All analysis has been carried out using data in a 4 cm square near the center of the field on 20.3 × 25.4 cm (8 × 10 inch) plates. Our analysis has assured us that adequate uniformity

TABLE 1
CTIO 4 m PRIME FOCUS PLATES ON NGC 5236 (M83)

Band (Emulsion/Filter)	Plate No.	Exposure Time (min)	Date (1976 June)	Seeing* (arcsec)	Average Air Mass	Maximum Calibrated Errors: Std. Dev. $D - I/(S.E.M.)$, P.E. zero pt.)	Valid <i>F</i> -Range (20% Sky); Valid mag Range; Typical Error
<i>U</i> (103a-O/UG2).....	2111	5	20/21	2.0	1.019	18-17540;	
<i>U</i> (103a-O/UG2).....	2095	15	19/20	2.0	1.015	24.35-16.89;	
<i>U</i> (103a-O/UG2).....	2096	50	19/20	2.5	1.079	0.03 mag	
<i>B</i> (103a-O/G385).....	2098	10	19/20	2.5	1.446	15-14500;	
<i>B</i> (103a-O/G385).....	2097	30	19/20	2.5	1.315	24.60-17.10;	
<i>B</i> (103a-O/G385).....	2112	45	20/21	2.0	1.064	0.015 mag	
<i>V</i> (103a-D/G495).....	2100	10	19/20	2.5	1.900	40-11530;	
<i>V</i> (103a-D/G495).....	2099	30	19/20	2.5	1.652	23.51-17.35;	
<i>V</i> (103a-D/G495).....	2114	30	20/21	2.5	1.252	0.015 mag	
<i>R</i> (998-04/RG610).....	2126	5	21/22	1.5	1.015	102-22300;	
<i>R</i> (998-04/RG610).....	2127	20	21/22	1.5	1.006	22.48-16.62;	
<i>R</i> (998-04/RG610).....	2116	45	20/21	2.5	1.548	0.02 mag	
H α (127-02/λ6565, 120 Å FWHM).....	2128	60	21/22	1.5	1.008	120-32768; 22.29-16.21†; { 0.05 mag	

* Estimated visual seeing during exposure; from scans, images of faint stars were $\sim 1''$ FWHM on all plates.

† H α magnitude scale is set to be identical with *R* magnitude scale, i.e., if an *R* photometer were placed on an H α line source, m_{Ha} is defined to equal m_R read by the photometer.

over the 4 cm square field from plate to plate has been achieved.

b) Photoelectric Photometry

Aperture photometry of M83 was obtained using the three-channel photometer with the 0.91 m CTIO telescope on the nights of 1976 June 28/29 through 1976 June 31/July 1. Calibrations were made with Landolt (1973) equatorial standards. The observations were of excellent photometric quality for only two of the nights, and only those data were used for the calibrations of the photographic plates. The data were analyzed with a three-color photometry reduction program essentially identical to the KPNO reduction program developed by B. Weymann. The combined data for the standard stars have standard deviations for their residuals of $\sigma(U - B) = 0.064$, $\sigma(B - V) = 0.016$, and $\sigma(V) = 0.019$ (for 16 standards), implying standard errors of the means for the zero points of $\lesssim 0.01$ mag. Further photometry was obtained using the single-channel photometer with the 0.61 m CTIO telescope on the nights of 1976 July 1/2 through July 4/5. Standard *BVR* filters and photometers were used, and calibrations were based on standards from Johnson (1963) and Kunkel (1976). The observations were of adequate photometric quality for only one night, and only those data were used for the calibration of the *R* photographic plates. Owing to the lower quality of the 0.61 m data, they were normalized to the 0.91 m data via the *V*-band so that the 0.61 m observations provide only the *V - R* colors, with $\sigma(V - R) = 0.017$ (for 10 standards). Using both telescopes, photometry was obtained for several apertures centered on the nucleus and for various regions in the galaxy chosen to be free of bright foreground stars. The regions used were selected from Sky Survey prints, and telescope positioning was achieved with the help of an offset-guider. The locations observed, apertures used, corresponding magnitudes, and colors are listed in Table 2.

To supplement the CTIO photoelectric photometry, additional *BVR* photometry was obtained by one of us (E. B. J.) on 1977 May 7/8 using the KPNO 1.3 m telescope with the fast-scan system (Strom *et al.* 1977). The scanning secondary of the telescope was aligned to yield 49 samples along the N-S axis of the galaxy,

with the nucleus centered at sample 11 at the south end of the scan. The sample spacing used was $14''.8$ with a diaphragm $30''.3$ in diameter. Owing principally to the very large zenith distance (always $\gtrsim 60^\circ$) at which it was necessary to work, no attempt was made to put these observations on a calibrated *BVR* system. However, they proved extremely useful in providing photoelectric confirmation of the accuracy of our *D-to-I* and sky-subtraction procedures, over about a 3.5 mag range in surface brightness. The fast-scan data, referred to the nucleus, are presented in Table 3. The errors are derived by propagating \sqrt{N} counting statistics; however, the principal source of error in these data is undoubtedly the error introduced by uncertain guiding, and probably amounts to 0.10 mag in some channels. Also, the data are uncorrected for color errors, which must certainly exist but which are not significant over the color range observed.

c) Photographic Photometry

All of the plates were scanned in identical fashion on an Optronics International microdensitometer at the NASA Johnson Space Center using a $40 \mu\text{m}$ square aperture with $40 \mu\text{m}$ steps and a 1000×1000 pixel raster. With the 4 m plate scale of $18''.6 \text{ mm}^{-1}$, this yields pixels $0''.74$ square on the sky. With typical seeing conditions, there are two to three pixels per linear resolution element. Faint stars were used to produce images properly registered to within less than one pixel over the whole 1000×1000 raster. Procedures were used which reduced distortion of stellar images and drift to negligible levels.

For each pixel, the density above fog, $D_i = d_i - d_{\text{fog}}$, was fitted to the known logarithms of the spot intensities, $y_i = \log_{10} I_i$. The fitting formula used (Tsubaki and Engvold 1975) was

$$\begin{aligned} y &= Y(D) = a_1 D + a_2 \ln [\exp(a_5 D) - 1] \\ &\quad + a_3 \exp(a_5 D) + a_4; \end{aligned} \quad (1)$$

the fitting procedure was to find the a 's by minimizing the function

$$\chi^2(a_1, \dots, a_5) = \sum_i [y_i - Y(D_i)]^2 \sigma_i^{-2}, \quad (2)$$

TABLE 2
PHOTOELECTRIC CALIBRATION REGIONS FOR NGC 5236 (M83)

REGION/APERTURE DIAMETER	OFFSET FROM NUCLEUS (arcsec)		SURFACE BRIGHTNESS (mag arcsec $^{-2}$)			
			<i>U</i>	<i>B</i>	<i>V</i>	<i>R</i>
B/33''.....	168 S	166 W	23.30	22.96	22.13	21.46
C/33''.....	42 S	43 W	20.08	19.27
E/33''.....	114 N	104 E	20.94	20.25
F/33''.....	144 N	192 E	23.36	22.98	22.24	21.53
I/33''.....	48 N	50 W	21.81	21.61	20.79	20.01
J/33''.....	37 S	35 E	21.73	21.47	20.68	19.80
K/33''.....	187 S	176 E	22.83	22.68	22.05	...
Center/7''.2.....	0.0	0.0	16.48	16.74	16.29	...
Center/33''.....	0.0	0.0	18.19	18.41	17.82	...

TABLE 3
1.3 m FAST-SCAN PHOTOMETRY FOR M83

SECTOR POSITION	BLUE		VISUAL		RED	
	Magnitude Difference	Statistical Error	Magnitude Difference	Statistical Error	Magnitude Difference	Statistical Error
162°8' S.....	3.59	0.01	3.50	0.01	3.52	0.02
148.0.....	3.31	0.01	3.29	0.01	3.28	0.02
133.2.....	3.18	0.01	3.20	0.01	3.23	0.02
118.4.....	3.27	0.01	3.28	0.01	3.31	0.02
103.6.....	3.39	0.01	3.29	0.01	3.33	0.02
88.8.....	3.30	0.01	3.14	0.01	3.15	0.01
74.0.....	3.19	0.01	3.04	0.01	3.06	0.01
59.2.....	3.05	0.01	2.81	0.01	2.81	0.01
44.4.....	2.71	0.01	2.42	0.00	2.41	0.01
29.6.....	2.32	0.01	1.91	0.00	1.92	0.01
14.8 S.....	0.60	0.00	0.50	0.00	0.52	0.00
0.0.....	0.00	...	0.00	...	0.00	...
14.8 N.....	0.64	0.00	0.61	0.00	0.61	0.00
29.6.....	2.31	0.01	1.94	0.00	1.92	0.01
44.4.....	2.78	0.01	2.42	0.00	2.41	0.01
59.2.....	3.04	0.01	2.76	0.01	2.77	0.01
74.0.....	3.16	0.01	3.00	0.01	3.04	0.01
88.8.....	3.53	0.01	3.27	0.01	3.29	0.02
103.6.....	3.62	0.01	3.39	0.01	3.38	0.02
118.4.....	3.47	0.01	3.37	0.01	3.38	0.02
133.2.....	3.31	0.01	3.35	0.01	3.38	0.02
148.0.....	3.39	0.01	3.48	0.01	3.53	0.02
162.8.....	3.49	0.01	3.58	0.01	3.61	0.02
177.6.....	3.59	0.01	3.67	0.01	3.70	0.02
192.4.....	3.62	0.01	3.68	0.01	3.71	0.02
207.2.....	3.78	0.02	3.78	0.01	3.79	0.02
222.0.....	4.07	0.02	4.01	0.01	4.03	0.03
236.8.....	4.20	0.02	4.07	0.01	4.11	0.03
251.6.....	4.58	0.03	4.52	0.02	4.54	0.05
266.4.....	4.65	0.03	4.78	0.03	4.77	0.06
281.2.....	5.35	0.06	5.15	0.04	5.24	0.09
296.0.....	5.54	0.07	5.38	0.05	5.35	0.10
310.8.....	5.61	0.08	5.53	0.05	5.49	0.11
325.6.....	5.87	0.10	5.75	0.06	5.59	0.12
340.4.....	6.34	0.15	6.12	0.09	6.00	0.17
355.2.....	6.57	0.19	6.45	0.12	6.06	0.18
370.0.....	7.12	0.31	6.78	0.16	6.61	0.30
384.8.....	7.32	0.38	7.05	0.21	6.73	0.33
399.6.....	7.40	0.41	6.96	0.19	6.62	0.30
414.4.....	8.10	0.90	7.12	0.22	6.81	0.36
429.2.....	8.51	2.58	7.68	0.38	7.82	1.21
444.0.....	7.34	0.39	7.54	0.33	7.54	0.80
458.8.....	9.17	∞	7.50	0.32	7.22	0.55
473.6.....	8.53	5.00	7.95	0.50	7.23	0.56
488.4 N.....	8.55	∞	8.04	0.55	8.44	∞

where the summation was over those spots which were distinctly above the fog and were unsaturated. The spots were weighted by setting $\sigma_i = 0.12$ mag for $D_i < 0.2$ or for $D > 3.0$ and $\sigma_i = 0.04$ mag for $0.2 < D_i < 3.0$. (These σ 's represent the purely random pixel-to-pixel variation, which is separate from the systematic uncertainties discussed below.) Files were then produced with pixel values equal to $f_{pg} = \text{dex}[Y(D)]$.

Each individual plate was placed upon the $UBVR$ photoelectric scale by doing simulated aperture photometry. Sky brightness values were first determined by use of special sky scans made far from the center of the galaxy. In addition, sky values were determined by fitting the photoelectric surface brightness μ_{pe} (mag arcsec^{-2}) to the fluxes produced by the density-to-

intensity (D -to- I) conversion. That is, for each plate we determine A and S in the following equation:

$$F_{pe} = \text{dex}[0.4(27.5 - \mu_{pe})] = Af_{pg} - S = F_{pg}. \quad (3)$$

Here S is the absolute surface brightness of the sky, $S = F_{pg}(\text{sky}) = \text{dex}\{0.4[27.5 - \mu_{pg}(\text{sky})]\}$. Unfortunately, we found small but statistically significant differences between the sky values S derived by the different methods. The differences amounted to about 4% in V and U , 2% in R , and 10% in B in the sense $S(\text{plate}) - S(\text{p.e.}) > 0$, but the differences were not consistent from plate to plate. These differences are small enough so as not to affect significantly the colors we derive over most of the galaxy, since the galaxy

brightness exceeds the sky brightness throughout almost all of the range in radius we consider. However, the differences are bothersome, for they are not in the sense that might naively be expected due to scattering in the prime-focus camera optics, the one major instrumental uncertainty for which we have no means of making quantitative corrections. It is not due to the pincushion distortion in the corrector, for we have incorporated this effect (Chiu 1976) into our analysis. We rejected the possibility that our photoelectric photometry could be the principal source of this discrepancy, because the discrepancies among different plates in each passband are comparable to the mean discrepancy between the photographic and photoelectric results.

Table 1 shows the standard deviation of the residuals for the $D - I$ fit, the standard error of the mean (s.e.m.) for the zero point of the photometry scale, and the range for which the calibrated images are valid. The separate images for each of the $UBVR$ bands were co-added. This reduced pixel-to-pixel noise and reduced the s.e.m. for the co-added calibrations. For pixels falling within the valid range, the co-added sum represents the mean of one, two, or three images, depending on how many are bright enough to be significant and also unsaturated. Individual plates have a range of about 5 mag; the use of overlapping plates extends the total range of each image to about 8 mag. The standard deviation of $D - I$ shown in the next-to-last column are worst case (one image only); over most of the magnitude range, the combination of images reduces this error by a factor of ~ 2 . The last column shows the final estimate for the typical systematic error for each final picture.

The final $UBVR$ images are on a linear surface brightness scale (F) which is directly related to the $UBVR$ photoelectric scale (μ) by

$$F = 10^{0.4(27.5 - \mu)}. \quad (4)$$

The systematic calibration errors are believed to be less than 0.05 mag s.e.m. for all μ , and they are probably less than 0.02 mag for most of the available magnitude range.

In addition to the calibration errors, the only remaining systematic errors we have considered are plate nonuniformity and adjacency effects. By comparing the four corners with the sky scans and S -values, the nonuniformity effects have been estimated to be less than 0.03 mag for the combined images (we have incorporated the geometrical distortion using data from Chiu 1976; it is only about a 0.01 mag correction at the corners of our scans). The only evidence potentially useful to evaluate adjacency effects comes from the shapes of stellar images and the shapes of the step transitions at the edges of the sensitometer spots. The primary influence of the adjacency effect appears to be that of spreading a point image in a fashion similar to spreading by seeing. To obtain adequate statistics we are always concerned with averages of pixels over regions large compared with these spreading effects.

The $H\alpha$ image is produced from the intensity rasters

made from the $\lambda 6565$ interference filter (FWHM = 120 Å) photograph and the red wide-passband photograph. The zero point is set by using the calibration regions for the R photoelectric photometry and finding the parameters A and S such that, for those regions free of $H\alpha$ emission,

$$F_{6565} = Af_{6565} - S = \text{dex}[0.4(27.5 - \mu_R)] = F_R. \quad (5)$$

Then we define for each pixel

$$F_{H\alpha} = \text{dex}[0.4(27.5 - \mu_{H\alpha})] = F_{6565} - F_R. \quad (6)$$

One can convert from $\mu_{H\alpha}$ to flux in ergs $\text{cm}^{-2} \text{s}^{-1}$, $f(H\alpha)$, by

$$\mu_{H\alpha} = -2.5 \log f(H\alpha) - 13.55, \quad (7)$$

using the zero point of the R magnitude system (Allen 1973).

III. $UBVRH\alpha$ SURFACE BRIGHTNESS AND COLOR

a) Two-dimensional Maps of Surface Brightness and Color

After calibration, the $UBVRH\alpha$ images on magnetic tape were taken to the KPNO Interactive Picture Processing System (IPPS; Wells 1975). With the Comtal color video display, we played back the intensity images and generated and played back new images from them, e.g., maps of $UBVRH\alpha$ magnitudes and maps of $U - B$, $B - V$, and $V - R$ colors. Figure 1 (Plate 3) displays calibrated $UBVR$ intensity maps, a calibrated $H\alpha$ intensity map, and a composite map of the $H\alpha$ distribution overlayed on a $B - V$ color map in which pixels bluer than $B - V = 0.65$ have been masked off. This last map was prepared to dramatize the association between the distribution of $H\alpha$ and the positions of the two principal dust lanes. The maps are all sky-subtracted logarithmic displays with 0.5 mag intervals shown at the top. The darkest (rightmost) calibration step is 18.0 mag arcsec^{-2} . Figure 2 (Plate 4) displays the color maps $B - V$ and $U - B$, and the approximately reddening-free parameter

$$Q \approx (U - B) - 0.72(B - V). \quad (8)$$

(See Appendix A for a discussion of the relationship between Q and interstellar reddening.) The color maps are displayed with 0.1 mag intervals shown at the top (at the bottom in the case of Q). The darkest (rightmost) calibration steps are $B - V = 1.1$, $U - B = 0.7$, and $Q = +0.3$. The maps in Figure 1 are 500×500 pixel displays obtained by compressing the original 1000×1000 pixel rasters by a factor of 2 so that they could be accommodated within the 512×512 format of the IPPS. The maps in Figure 2 are instead 512×512 extractions from the centers of the original rasters, in order to show more clearly the details of the structure of the center portion of this galaxy. A burned out region at the nucleus, of varying size from map to map, is displayed as blank.

b) One-dimensional Presentation of Spatial Information

In order to more readily assimilate whatever intelligible content may be present in our two-dimensional intensity and color distributions, and in order to compare our data with those of other observers, it is necessary to sum our data into appropriate one-dimensional forms. In Figure 3, photoelectric aperture photometry for NGC 5236 by Pettit (1954), Westerlund and Wall (1969), de Vaucouleurs (1961), and Alcaino (1974), along with our two sets of photoelectric measurements centered on the nucleus, has been displayed along with simulated "aperture photometry" obtained by summing the pixel values within the appropriate circular areas of our rasters. The agreement between our photoelectrically calibrated photographic photometry and the photoelectric photometry of these other observers appears satisfactory.

In order to investigate the physical processes within the galaxy, it is desirable to have radial profiles corrected for inclination and projection effects. Estimates of the inclination vary greatly; by comparing the major and minor axis radii at various isophotes, values in the range of 13° – 24° may be obtained (Danver 1942; Rogstad, Lockhart, and Wright 1974; RC2), while, on the other hand, Danver (1942) deduced a value of 46° from his least-squares fit of logarithmic spirals to the spiral arms. Here we somewhat arbitrarily adopt the value $i = 24^{\circ}$, corresponding to the RC2 value; no

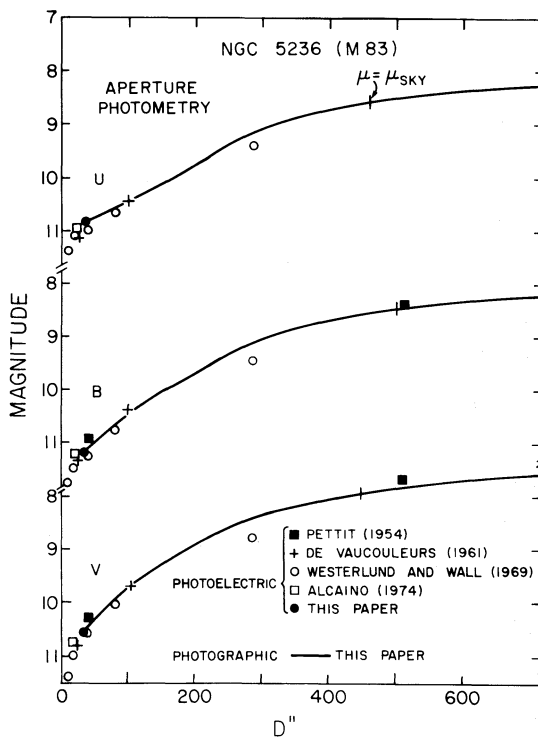


FIG. 3.—Comparison of simulated aperture photometry on our photographic data with published photoelectric photometry. The UBV magnitudes are shown plotted versus circular aperture diameter.

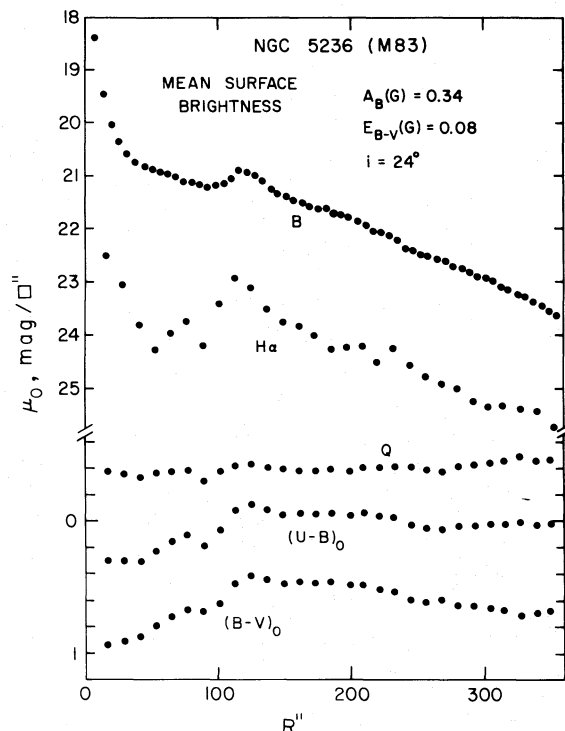


FIG. 4.—Azimuthally averaged fluxes in annular zones in the plane of the galaxy (inclined 24° to the plane of the sky) are displayed for the B and $H\alpha$ passbands, along with $(U - B)_0$, $(B - V)_0$, and Q colors derived from the averaged fluxes. The subscript 0 denotes quantities corrected for Galactic extinction $A_B = 0.34$ and for M83's inclination ($\cos 24^{\circ}$).

result in this paper is strongly dependent on this choice. Using this choice and the major-axis position angle of 45° , we have binned the data into a polar coordinate system in the plane of the galaxy, multiplying the fluxes by $\cos i$ to correct for projection, assuming a thin disk. We have employed 90 azimuthal bins and 60 radial zones ($\Delta r = 8$ pixels = $5'95$). Data contaminated by obvious foreground stars were omitted in the binning process. Averaging over θ then yields radial profiles, which we have displayed in Figure 4, of the quantities μ_{B0} , $(U - B)_0$, $(B - V)_0$, $\mu_{H\alpha}$, and Q . The subscripts 0 indicate quantities corrected for Galactic obscuration where we have adopted $A_B = 0.34$ (from RC2), $R = A_V/E(B - V) = 3.3$, and $U - B$ is corrected in the fashion discussed in Appendix A. Note that the inclination correction is purely geometrical, and it does not include any correction for inclination-dependent internal obscuration. The surface brightness and color profiles clearly show the well-known exponential disk characteristic of spiral galaxies. The disk is remarkably close to an exponential from $r = 130''$ out to about $r = 350''$, the limit to which we have analyzed our material. The $U - B$ and $B - V$ colors show that the regions inside and outside of the $120''$ jump are significantly different in character as well as in surface brightness.

c) RC2 Catalog Data

From our extensive photoelectric photometry and large 4 m plate collection we should presumably be able to deduce the RC2 photometric parameters with more accuracy than was possible with the data available to the original compilers of the catalog. We have derived RC2 photometric parameters for M83 based on our data, and we present the results in Table 4. It should be noted that several parameters we have derived are extrapolations based on an exponential fit to the data between $r = 140''$ and $r = 340''$. Also, several of the parameters include corrections for the inclination dependence of the internal obscuration. For this table only, we have adopted the RC2 prescription for this correction which is based on the statistical properties of galaxies of this type. We have used the inclination $i = 24^\circ$ based on ellipticity of faint isophotes so that the results are compatible with RC2.

d) Availability of the Full Set of Digital Data

The full set of data is published here only as calibrated gray-scale maps. For almost any kind of analysis, one generally needs the actual digital data. Printing the entire data set is costly, and the data are essentially useless in that form anyway. Their value lies principally in the possibility of computer processing the large data base. Consequently, since we have the full set of F_U , F_B , F_V , F_R , and $F_{H\alpha}$ data on magnetic tape, we have decided to supply interested investigators with a copy of the tape. This will be available for 24 months following date of publication. Contact the first author for details. At a referee's suggestion, we have deleted from our discussion many of the details of the data analysis procedures. These will be supplied with the description of the contents of the tape. In Appendix B, we provide tabular data for a subset of the averaged data, in the hopes that these will be sufficient for interested investigators to experiment with and to obtain a feel for handling such data.

IV. AZIMUTHAL AND RADIAL DISTRIBUTION OF SURFACE BRIGHTNESS AND COLOR

Figure 5 shows the blue surface brightness μ_{B0} and the $(B - V)_0$, $(U - B)_0$, and Q colors plotted as a function of radius. Each point on the plot represents a square region about 3" on a side. The scatter in each of the four plots at a given radius is due almost entirely to the azimuthal variation of the plotted parameter at that radius. Four regions of the profiles are labeled *A*, *B*, *C*, and *D*. Interior to region *A* and not shown here or on our intensity and color maps in Figures 1 and 2 is the nuclear region, about 20" across, which attains $\mu_B \sim 16$, $(U - B)_0 = -0.51$, and $(B - V)_0 = 0.18$. This nuclear "hot spot" is a well-known complex of young stars and H II regions (Evans 1956). Region *A*, starting just outside the bright nuclear region, is a region of steeply falling surface brightness that approximately follows the de Vaucouleurs $r^{1/4}$ law for spheroidal components. Region *C* consists of a distinct "hump" in the intensity profile; it also contains the bluest light

TABLE 4
NGC 5236: NEW RC2 PARAMETERS

Parameter	RC2 Column/Row	Value
$\log D_0^*$	12/2	2.21
$\log A_e$	13/1	1.71 ± 0.02
B_T^*	16/1 + 2	8.24 ± 0.03
m_e^*	17/1	12.28
m_{25}^*	17/2	14.04
B_T^0	18/2	7.87
$(B - V)_T$	19/1 + 2	0.66 ± 0.03
$(U - B)_T$	20/1 + 2	0.03 ± 0.03
$(B - V)_e$	21/1 + 2	0.66 ± 0.03
$(U - B)_e$	22/1 + 2	0.03 ± 0.03
$(B - V)_T^0$	23/1	0.57
$(U - B)_T^0$	23/2	-0.03

* These are computed using exponential fit to μ_B^0 to extrapolate beyond $r = 340''$: $\mu_B^0(r) = 19.75 + r/93''.0$.

in the galaxy outside the nucleus and the largest scatter in intensity and color. The region *D* beyond the "hump" is also quite blue, and it is evident from the color maps that the blue colors of these regions are due to the presence therein of active, recent star formation.

We have plotted in Figure 6 azimuthal profiles of the same quantities shown in Figure 5 at two fixed radii (in the plane of the galaxy), 100" and 160". Each point plotted represents a 1.5" square pixel; all of the points that lie within 3" wide annuli are plotted. (Portions of two star images appear on the $r = 100''$ profile.) Each of the relatively sharp minima in μ_B corresponds to a dust lane or spur in the galaxy. They are not "black"; i.e., the typical faintest μ_B for $r = 100''$ is 22.0 mag arcsec $^{-2}$, which was about twice the brightness of the sky. The two major dust lanes, which are among the most striking morphological features of this galaxy, are marked in the figure. It is interesting that they are relatively prominent in photographs only because of their long, coherent nature. In the azimuthal plots they are not conspicuous. The azimuthal profiles are consistent with a simple picture of the structure of spiral galaxies, in which optically thick dust lanes concentrated in the central plane obscure the even more centrally concentrated young associations. The dust lanes produce sharp drops in surface brightness, but in no case do these drops exceed 0.75 mag.

In order to evaluate the effect of the obviously vigorous, recent star formation on the radial intensity profile, we have performed a primitive population separation, based on the $B - V$ colors, of the pixels plotted in Figure 5. Simple calculations based on evolving cluster models such as those of Tinsley (1968) and Searle, Sargent, and Bagnuolo (1973) suggest that for a pixel to be bluer than $B - V = 0.4$ the stellar birthrate in the recent ($t < 10^8$ years) past must have been greater than about twice the mean of the past rate. On the other hand, if the color is redder than $B - V = 0.65$ then the recent birthrate must be less than about one-seventh of the mean, neglecting reddening. This calculation led us to plot in Figure 7

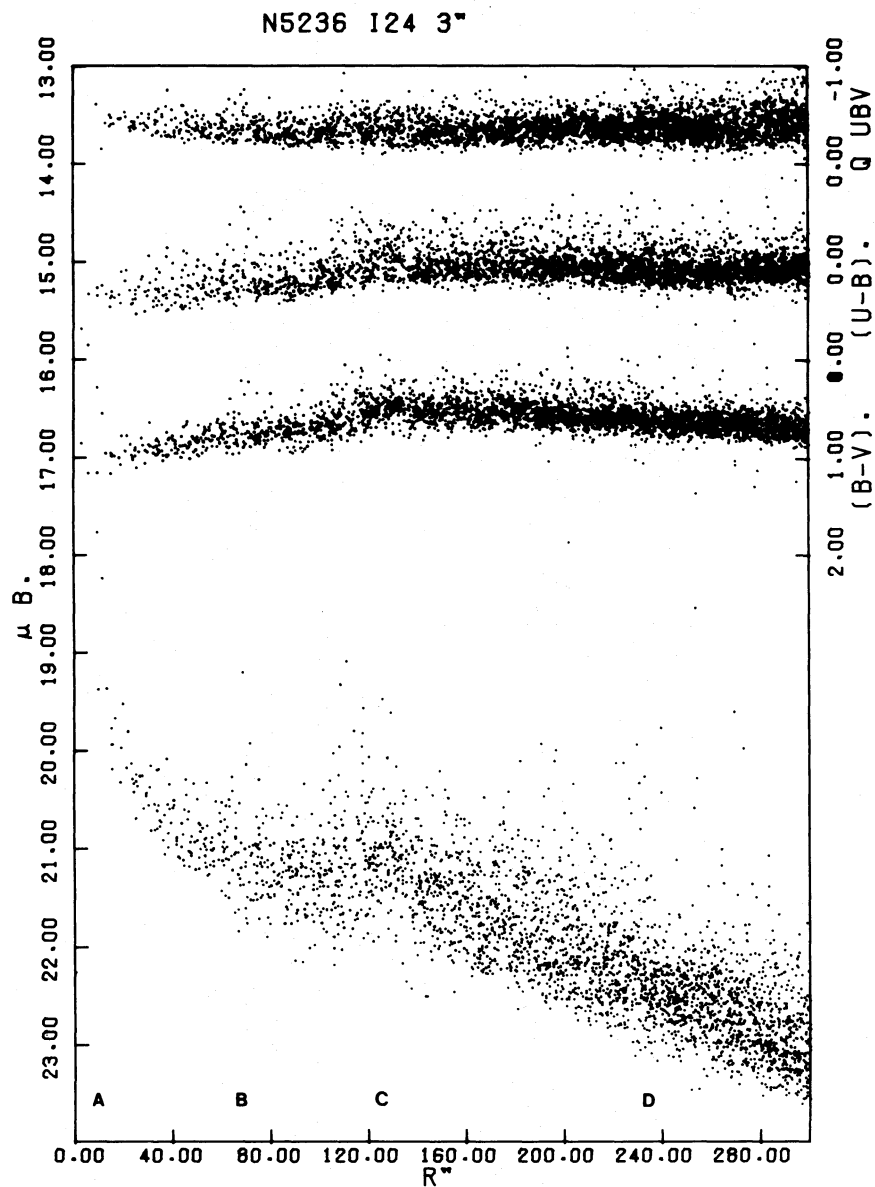


FIG. 5.—Plots of μ_{B0} , $(U - B)_0$, $(B - V)_0$, and Q for individual 3'' square pixels versus radius in the plane of the galaxy inclined at $i = 24^\circ$. The error in each data point is < 0.05 mag in all cases and is usually $\lesssim 0.01$ mag; the scatter is real variation with azimuth. Occasional bright points are foreground stars. To avoid overcrowding, a random selection of only one point in 10 is plotted.

a random selection of the bluest ($B - V < 0.40$, shown as Y for young) and reddest ($B - V > 0.65$, shown as O for old) pixels. To minimize crowding, only one-fifth of the blue points and 1/15 of the red points are shown. The most striking, and to us unexpected, characteristic of this plot is the complete disappearance of the “hump” in the profile defined by the O pixels. This apparently implies that the existence of the “hump” in the integrated B profile is due solely to the contribution to the integrated light from the very inhomogeneously distributed young stars. The faintest pixels at each radius are generally those in dust lanes, where almost exactly one-half of the disk light and all

of the young light is obscured. Then the mean disk surface brightness must lie very nearly 0.75 mag above this lower envelope. Few pixels can be expected to be attenuated by more than about 0.75 mag, which is why the lower envelope of the red pixel distribution is so well defined.

Because of the presence of the feature we have labeled the “hump,” Freeman (1970), in his study of the disks of spiral and lenticular galaxies, classified M83 as Type II—in fact, M83 was Freeman’s prototype for the Type II profile. However, the residual profile after removal of the contamination from the inhomogeneously distributed young light has a

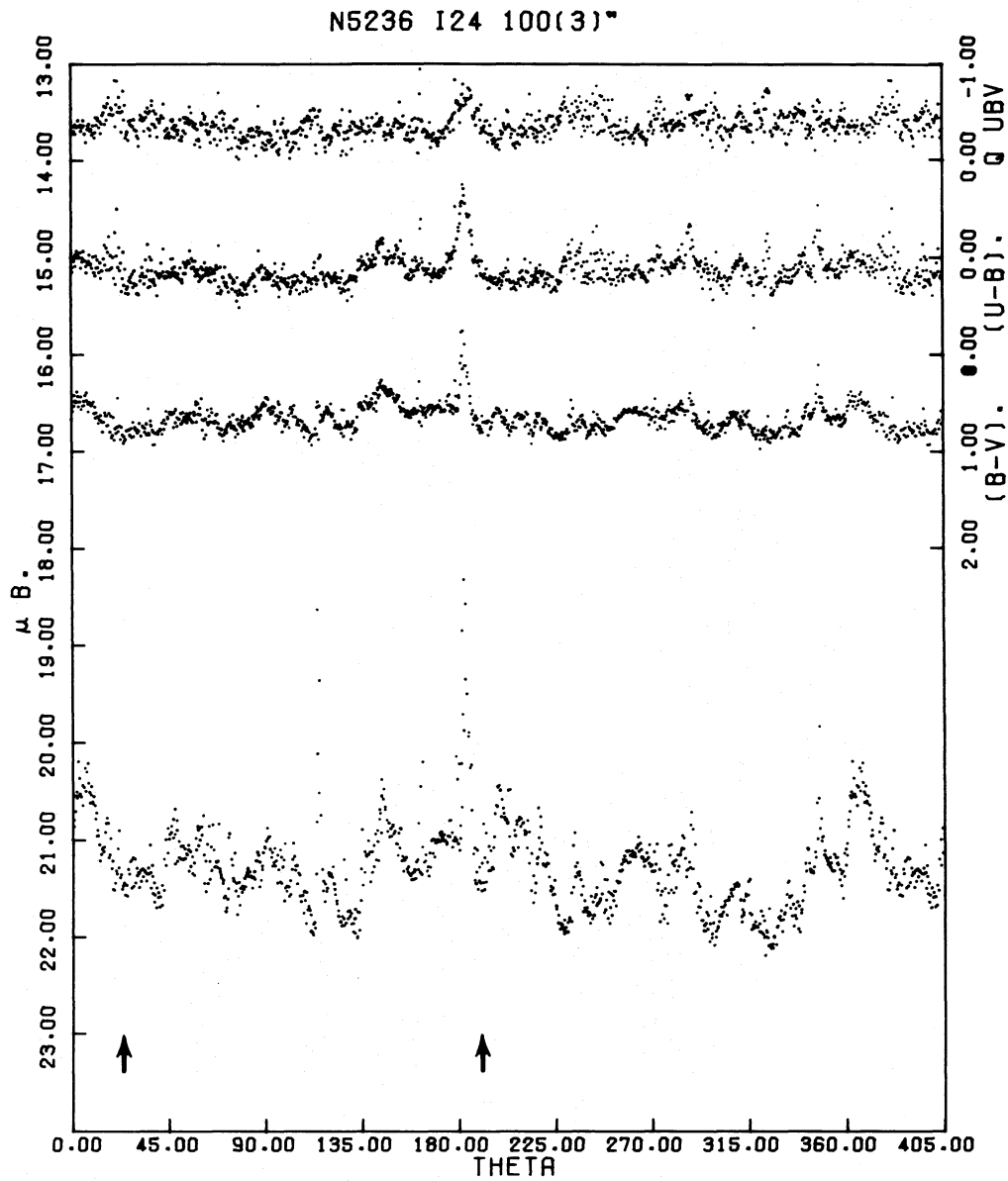


FIG. 6a

FIG. 6.—Azimuthal plots of data in two annular rings 3'' wide. $\theta = 0^\circ$ is at $PA = 45^\circ$ (measured counterclockwise from North), and θ increases counterclockwise. (a) $r = 100''\text{--}103''$; (b) $r = 160''\text{--}163''$.

monotonically decreasing surface brightness with a long “exponential” region, like that of a typical spiral galaxy of Freeman Type I. Evidently, the nature of the profile is entirely due to the radial distribution of bright blue patches of light, and it is in no way indicative of missing matter or a strange distribution of angular momentum per unit mass at the time the galaxy formed.

We have performed two additional measurements on our data in order to confirm this conclusion regarding the nature of the radial profile. In the first, working at the IPPS, we selected 19 small (6'' square) areas in the interarm regions of the galaxy by blinking between

the $B - V$ map and the μ_B map to find relatively smooth, relatively bright regions apparently free of extinction, but still substantially redder than the regions of star formation in the arms. Thus our selection combined “local” and “global” morphological criteria with a color criterion. The mean $(B - V)_0$ for the 19 samples was 0.67 ± 0.06 (standard deviation of sample means), while the mean Q was -0.24 ± 0.05 (standard deviation of sample means). As expected, these IPPS samples by and large fell along the upper envelope of the red pixels in Figure 7, even in the radial range of the “hump.” In a second test, we produced a plot in the same fashion as we produced

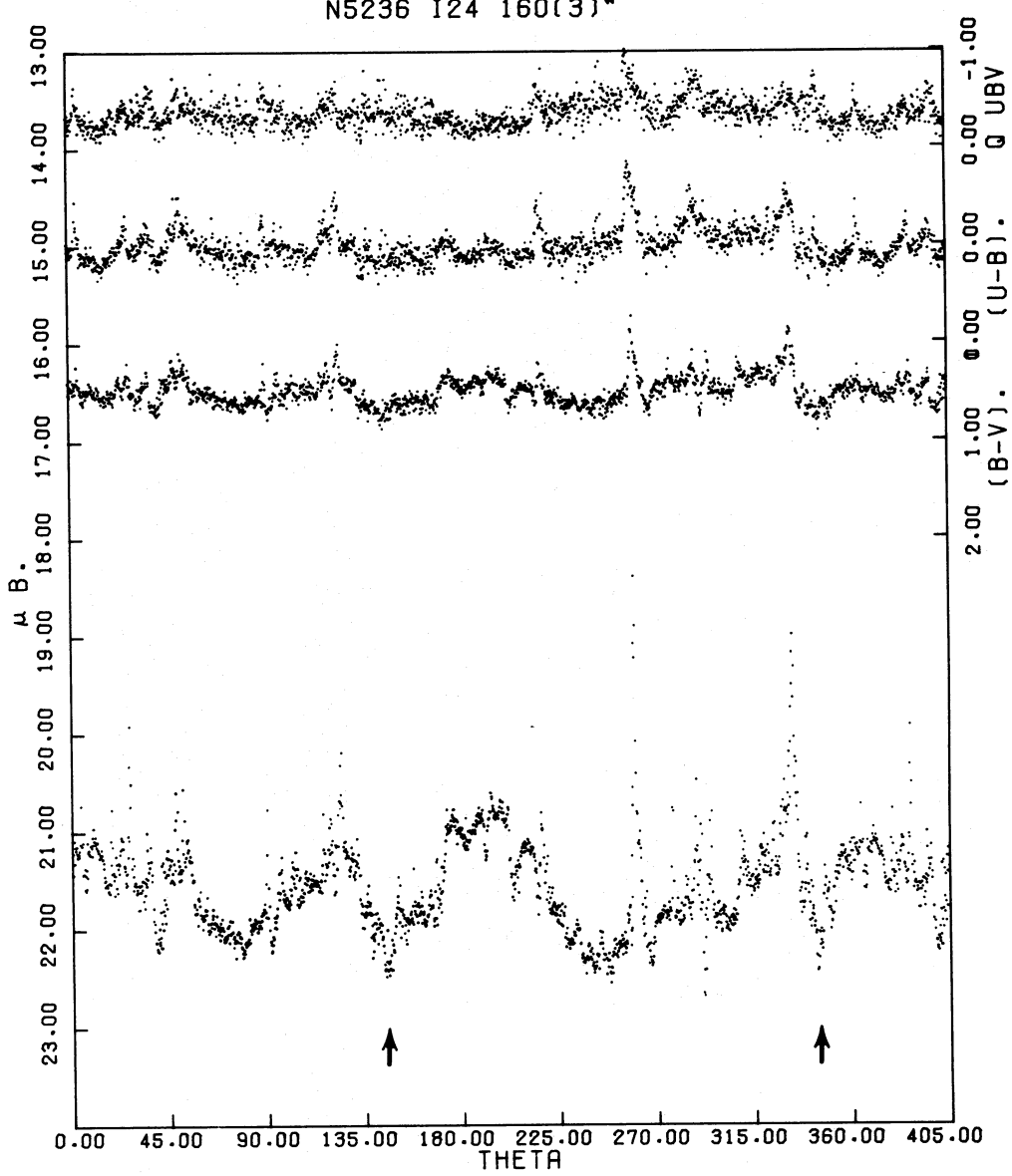


FIG. 6b

Figure 7, except that we selected pixels with $(B - V)_0 < 0.8$ and $Q > -0.3$, intending by this dual selection process to reject most pixels with significant star formation ($Q < -0.3$) and most pixels with significant reddening, $(B - V)_0 > 0.8$. Again, the result was a smooth, almost exponential profile without evidence for a "hump."

We have therefore established that in the case of M83 the existence of a Freeman Type II profile is due solely to the nonhomogeneous contribution to the integrated light from recent star formation. It is not completely clear how readily this explanation can be employed to explain other Type II profiles, however. We feel it is very likely that the same cause will serve to explain Type II profiles in other late spirals with vigorous star formation, such as NGC 224, NGC 6744,

and NGC 7793 in Freeman's original list. Among the other galaxies classed as Type II in Freeman's list, one (NGC 4526) seems to show evidence of internal dust on the plate published in the Hubble Atlas (Sandage 1961), while, as Kormendy (1977b) has pointed out, several others are almost edge-on, and there is reason to doubt the accuracy of some of the photometry Freeman employed. On the other hand, Kormendy (1977a, b) has found the profile of at least one galaxy, VII Zw 303, to be of Type II, while this galaxy's very red color ($B - V = 0.97$) and smooth appearance on the photograph published by Kormendy make it unlikely that either recent star formation or inhomogeneous internal absorption could be the cause of the inflection point in the profile. Furthermore, Gallagher (1978) has obtained two-color surface photometry of

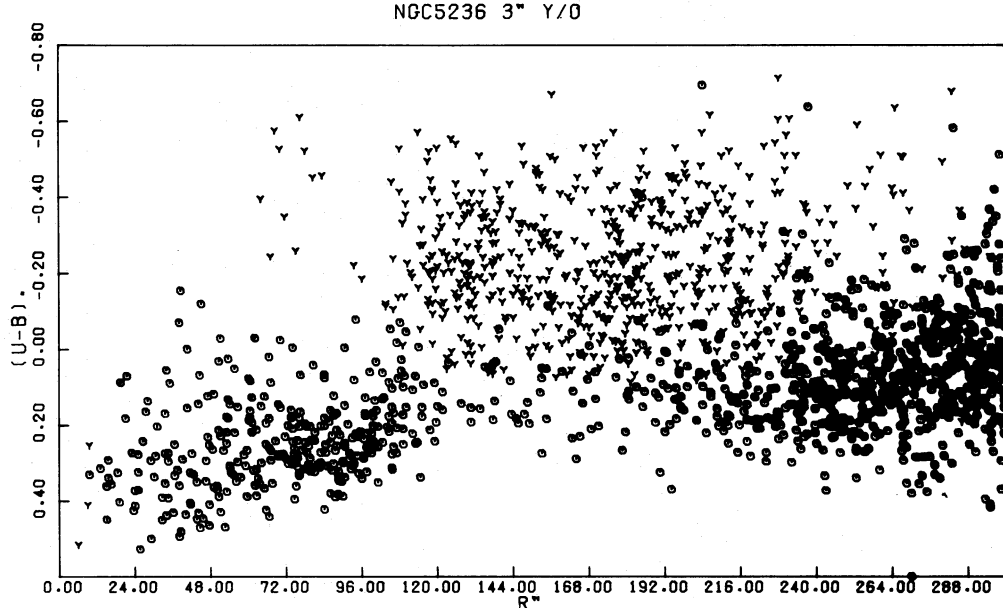


FIG. 7a

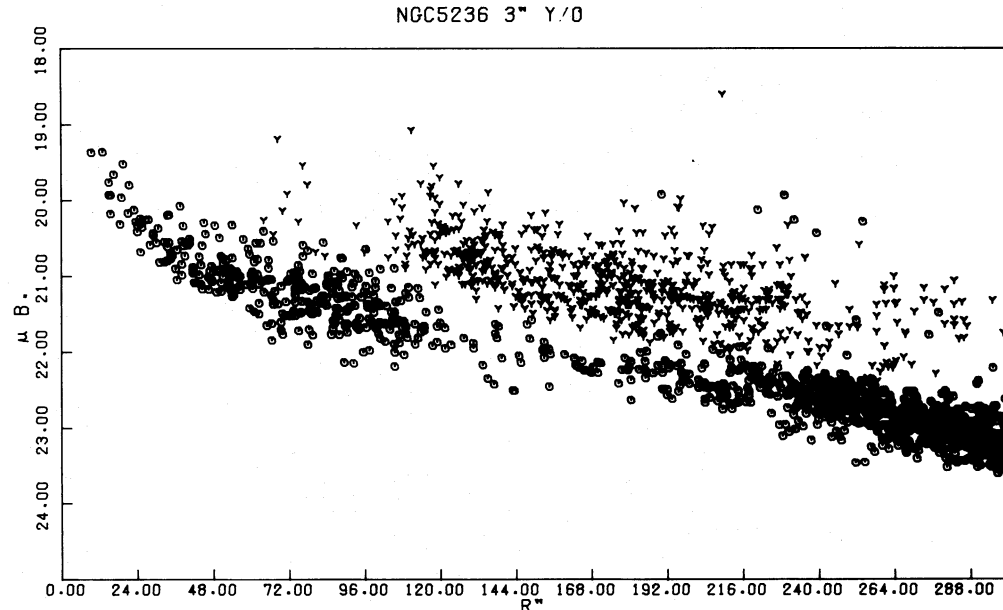


FIG. 7b

FIG. 7.—(a) $(U - B)_0$; (b) μ_{B_0} , for pixels selected on the basis of their color. “Old light” pixels $[(B - V)_0 > 0.65]$ are shown as O’s, and “young light” pixels $[(B - V)_0 < 0.40]$ are shown as Y’s.

three “outer ring” galaxies, NGC 1291 (which was also on Freeman’s list), NGC 1326, and NGC 2217, and he has found that although the “outer rings” (actually, weak spiral structure) are bluer than the interior regions of these galaxies, the star formation implied is insufficient to explain completely the inflection points observed in the profiles. Thus it seems fairly well established, despite our results for M83, that at least some disk galaxies exist with Type II profiles that have some dynamical significance.

V. THE ELUSIVE DRIFT VELOCITY

As has been pointed out by various students of spiral structure (e.g., Schweizer 1976; Larson 1977), and as we mentioned in our introduction, one of the strongest motivations for carrying out multicolor surface photometry of the kind we have presented in this paper is to permit an observational test of the density-wave hypothesis that the spiral-arm phenomena, including the associated star formation, are the

manifestations of a wavelike disturbance in the gravitational potential that propagates through the material of the galaxy, so that the locus of current star formation passes through the material of the galaxy in a smooth and presumably measurable manner. One would think that this motion of the spiral pattern should be easily recognized from the existence of strong and pervasive asymmetries in the appearance of the spiral arms, in both the intensity and color maps we have presented. Furthermore, from measurements of the "strengths" (slopes) of the asymmetries, the drift velocity of the (presumed rigidly rotating) pattern relative to the material as a function of radius ought to be calculable, and, with the help of a rotation curve, the "pattern speed" Ω , could then be derived.

Previous attempts to carry our observational tests for drift velocity, however, have failed to turn up convincing evidence for its existence. Dixon (1971) was able to measure a change in the ratio of blue to red supergiants in the direction perpendicular to a small section of the southern arm of M33; however, his sample was small, and merely from counts of supergiants, he could not quantify the drift observed. Schweizer (1976) searched his azimuthal intensity profiles for asymmetries in the arms; asymmetries in the expected sense outnumbered those in the opposite sense, but in most cases the intensity profile is rather broad and symmetrical, showing no evidence for a systematic gradient across the arm. Furthermore, when Jensen (1977) constructed two-color ($U - O$) profiles from Schweizer's published intensity profiles for M101, he found no greater tendency for asymmetries to exist in the vicinity of the arms than Schweizer had found from the intensity profiles alone.

Since M83 provides us with one of the most striking examples in the sky of the dust lane \rightarrow H II regions \rightarrow blue stars asymmetry (see Fig. 1f), and because our data are somewhat superior in resolution and signal-to-noise ratio to those previously employed in analyses of spiral structure, it was our hope that the detection and measurement of the drift velocity that has eluded earlier workers would be possible in M83. However, neither the azimuthal plots such as those in Figure 6 nor the intensity and color maps in Figures 1 and 2 reveal any obvious sign of asymmetry in the vicinity of the arms, other than the abrupt termination of star formation at the inside edge of the arms. The *outside* edges of the patches of star formation in the arms appear to terminate almost as abruptly as the inside edges, with little if any transition region of intermediate color and intensity such as one would expect in the naive "drift" picture. Thus the color maps, particularly the Q map, whose colors are quite insensitive to reddening, present an essentially two-tone appearance, showing large regions of vigorous and evidently near-synchronous star formation, mostly but not solely in the arms; regions of smooth red color where obviously little star formation is occurring, mostly between the arms; and little of intermediate color. A statistical analysis of the spatial variation of Q , described below, merely bears out this conclusion, obvious from inspection of the maps. In the broad-band colors (excluding the H α distribution),

there is *no sign of drift motion* in the vicinity of the arms.

The difficulty of finding evidence for drift velocity in the vicinity of the arms of M83 is not an embarrassment for the density wave theory, even though discovery of evidence for drift would nonetheless be strongly corroborative of the theory. Two effects, one quite obvious and one less so, can be plausibly expected to collude in such a way as to mask all obvious evidence of drift in the vicinity of the arms, even if the sole triggers for star formation in the galaxy are the two prominent dust lanes, and the spiral density wave picture is valid. The two effects are the spread in the time scale associated with star formation in clouds once they have been shocked, and the substantial radial component in the orbital motions of all material, but particularly cloud material, in the vicinity of the spiral arms. The first of these two effects acts to smear out the evidence for drift for ages up to a few times the spread. The second effect acts to crowd the drift into a much smaller angular region than would be expected based on the naive picture of circular orbits. Wielen and Schwerdtfeger (Wielen 1976) and Bash, Green, and Peters (1977) have calculated the orbits of objects in a spiral potential with initial conditions thought to be appropriate to gas at the solar radius in our Galaxy, just before it encounters the two-armed spiral shock wave. Wielen's calculations, based on the solar-neighborhood density-wave model of Yuan (1969), in this case predict that such objects will fall inward and actually recross the shock front after about 10^8 years, before finally leaving the vicinity of the spiral arm. So, as pointed out by Yuan (1977), even using a rather conservative estimate of 10–20 million years for the spread in star formation subsequent to the passage of the clouds through the shock (Woodward 1976), such extreme crowding of young stars in the vicinity of the arms would obliterate all trace of color evolution for stars younger than about 10^8 years, i.e., all of the stars that contribute significantly to the prominent blue patches in the $U - B$ and Q maps.

We thus find ourselves able to explain adequately the principal features of the color maps we have presented on the basis of the density-wave theory without having found in the maps any direct evidence for the grossly asymmetrical underlying situation that the theory predicts. We have found this situation to be so aesthetically displeasing that we have felt compelled to dig deeper into the data in the hopes that we could yet devise an observational test from which the theory would be unable to wiggle free. In order to do this we have considered the relatively smooth, red interarm regions, where the "signal" is the relatively young light older than about 10^8 years. Although this signal is enormously weaker than in the arms, and in these regions there may be confusion by star formation unrelated to the density wave, the density-wave theory makes an apparently unambiguous, unconditional prediction of systematic aging of the young stars, i.e., systematic reddening of their color.

A simple calculation was performed to test whether

plausible assumptions concerning the amount of star formation now occurring in the arms of M83 compared to the long-term star-formation history would lead to predictions of a detectable color gradient in the interarm region. The integrated colors of M83 (from Table 4) are consistent with an exponentially decreasing star-formation rate such that the present rate is about one-tenth the initial rate (e.g., using models of Searle, Sargent, and Bagnuolo 1973), while the colors of the annulus $125'' < r < 140''$ [$(U - B)_0 = -0.17$, $(B - V)_0 = 0.35$] are consistent with a nearly constant star-formation rate over 10^{10} years, assuming a Salpeter Initial Mass Function (IMF). Therefore, it is plausible to expect that the current star-formation rate in this annulus lies somewhere in the range roughly bracketed by the mean past rate and about one-fifth the mean past rate. If the bulk of the star formation occurs in bursts spaced by ~ 100 million years, and if the age of the galaxy is 10^{10} years, then the amount of star formation in each burst amounts to $1/100 - 1/500$ of the total previous star formation, and we can estimate the effect on the local color of the galaxy by adding the luminosity from a burst of this strength to that of an exponential model whose color matches that of the interarm region. The germane results from this calculation are tabulated in Table 5, which shows the total Q color evolution in a pixel 60 million years and 100 million years after bursts of star formation of strength 1/100 and 1/500. The residual color changes this long after the star-formation burst are small, but are still on the verge of what we could hope to detect in our data. However, the amount of the residual color change is highly sensitive both to the amount of time the young stars spend in the vicinity of the arms and to the IMF; a cluster with a "high-mass enriched" IMF dims much more rapidly than a cluster with relatively fewer massive stars.

To undertake this analysis we organized the Q data into a spiral coordinate system in the plane of the galaxy, where $\theta = 0$ is defined by the center of the strong dust lane in the east arm and θ increases counterclockwise. (We performed the analysis only over a range in r for which the east arm dust lane is strong.) We binned the data into radial zones in the plane of the galaxy and calculated least-squares slopes for Q as a function of θ in 30° ranges, using 24° for the inclination and a major-axis position angle of 45° . We were thus analyzing the data in sectors which in the plane of the sky were bounded by ellipses on the inside and outside and by projected logarithmic spirals on the other two sides. Before evaluating the results, we rejected all such sectors any part of which overlapped a dust lane or which lay more than 100° counterclockwise from a dust lane, thus excluding from consideration the arm regions. We then plotted the boundaries of our sectors on $U - B$ and Q maps of the galaxy, and used these maps to reject those additional sectors, within the interarm regions, in which we could identify sites of recent star formation. These star-forming regions are obvious in the $U - B$ and Q color maps in Figure 2 as distinct patches of blue light scattered about the interarm region. From

TABLE 5
RESIDUAL Q COLOR EVOLUTION*

STRENGTH OF BURST	TIME SINCE STAR-FORMATION BURST	
	60 m.y.	100 m.y.
1/100.....	0.08	0.03
1/500.....	0.03	0.01

* Change in Q from a time following a burst of star formation until the burst fades into indetectability against a galaxy model with exponentially decreasing star formation with a time scale of 2.2×10^9 years.

the integrated colors and shapes of these patches it is clear that they are preponderantly due to relatively small star-formation events recent compared to the last passage of the material through the arm. Star formation is so ubiquitous over the face of M83 that few of the 30° sectors, typically only two or three per radial zone, remained for further analysis. Most of the sectors that we rejected, including, of course, those in the arms, showed statistically significant slopes, but without any systematic correlation among sectors. Of the few zones that were not rejected because of obvious recent star formation, none showed significant slopes of either sense. Since the smallest significant slopes we found in any of our data were about that predicted by the "most favorable" model, in which the star-formation rate is still equal to the mean rate and the stars leave the vicinity of the arms within 60 million years of their formation, this appears to be a mildly significant result, constraining somewhat the IMF in the arms and the nature of the stellar orbits if the drift velocity hypothesis is correct. However, an additional complication predicted by the density-wave theory, which will be necessary to consider in a more accurate treatment of this problem, is the larger amplitude of the density wave in the relatively young stellar population, owing to its smaller velocity dispersion. This will produce a small but perhaps nonnegligible color gradient in the interarm region preceding the shock, of opposite sign to the gradient we seek to measure, and may be contributing to our nondetection of a color gradient between the arms. Further work on these ideas, involving the development of more elaborate star-formation models built with episodic rather than continuous star formation (Davis, Talbot, and Jensen 1978) is being pursued, and should lead to a better understanding of how star formation is proceeding in M83, even though it is likely, owing to the complications we have discussed, that it is not possible even in principle to obtain from these data the kind of clear-cut evidence concerning the drift that we have sought.

VI. CONCLUSIONS

We have presented calibrated maps of $UBVRH\alpha$ surface brightness and colors for NGC 5236. We have employed color and morphological information to remove the effects of recent star formation from the radial profile of surface brightness. This procedure

eliminates the "hump" which is characteristic of Freeman's (1970) Type II profile, leaving a smooth profile indistinguishable from Freeman's Type I. We have searched for systematic color gradients across and behind the spiral arms. Within the arms no systematic gradient is found, in agreement with expectations when proper allowance is made for noncircular orbits and imperfect synchrony of star formation. Behind the arms, those regions completely free of stars less than 50 million years old show no significant color gradients; this appears to put a weak constraint on the IMF and/or the amount of time young stars remain in the vicinity of the arms if the drift velocity hypothesis is correct.

We are developing an interpretation of the brightness and color distributions we have derived by comparing them with models of evolving stellar systems. In addition, we are analyzing H II region spectra to determine the distribution of their physical and chemical properties. It is our hope that it will prove possible to tie these observations together in a theory

relating current star formation, star formation history, and chemical composition of the gas. This work will be reported in future papers of this series.

We wish to thank the director and the staff of CTIO, particularly John Graham, Bill Kunkel, and Jim Hesser, for hospitality and useful discussions. The Kitt Peak Interactive Picture Processing System was essential for this work. We wish to thank Bob Milkey, Don Wells, and other members of the Kitt Peak staff who assisted us in its use. We gratefully acknowledge the assistance of the Kitt Peak Photo Lab, and we are also grateful to Bob Gooding of Technicolor Graphics Incorporated at the Johnson Spacecraft Center for use of the Specsca.

We wish to thank those many of our scientific colleagues who have encouraged us in this effort, particularly Don Clayton for his early and enthusiastic support. Finally, support by National Science Foundation grants AST 76-20076 and AST 78-00924 has made completion of this work possible.

APPENDIX A

REDDENING IN THE $(U - B, B - V)$ PLANE AND THE REDDENING-FREE PARAMETER Q

In the two-color plane, the slope of the reddening line $X = E(U - B)/E(B - V)$ is not constant, due to the well-known color dependence of the effective wavelengths of the broad-band U , B , and V passbands. As an approximation sufficient for our purposes, we adopt the following prescription, based on the investigation by Racine (1973):

$$\begin{aligned} X(B - V) &= 0.72 && \text{for } (B - V) < 0.60, \\ &= 0.72 + 1.65[(B - V) - 0.60] && \text{for } 0.60 < (B - V) < 0.77, \\ &= 1.00 && \text{for } (B - V) > 0.77. \end{aligned} \quad (\text{A1})$$

If X were constant at 0.72, then the reddening-free parameter $Q = (U - B) - 0.72(B - V)$ would be useful. It is merely the distance parallel to the $(U - B)$ axis from a point in the two-color plane to the reddening line of constant slope $X = 0.72$ which passes through $(0, 0)$. However, that line, as all other reddening lines, changes slope (eq. [A1]); consequently, instead of that reddening line given by

$$(U - B)_{00} = +0.72(B - V),$$

one has that line being given by $(U - B)_{00} = W[(B - V)]$, where

$$\begin{aligned} W &= +0.72(B - V) && \text{for } (B - V) < 0.6, \\ &= 0.298 - 0.27(B - V) + 0.825(B - V)^2 && \text{for } 0.6 < (B - V) < 0.77, \\ &= -0.192 + 1.00(B - V) && \text{for } (B - V) > 0.77. \end{aligned} \quad (\text{A2})$$

We now define Q to be again the distance measured parallel to the $(U - B)$ axis; i.e.,

$$Q \equiv (U - B) - (U - B)_{00} = (U - B) - W[(B - V)]. \quad (\text{A3})$$

The computation of $(U - B)_0$ and $(B - V)_0$, the values corrected for reddening, is possible if one has determined $E(B - V)$. By definition,

$$(B - V)_0 \equiv (B - V) - E(B - V) \quad (\text{A4})$$

and

$$Q_0 \equiv Q \quad (\text{A5})$$

(the latter is the condition that the reddening lines are parallel in the $[U - B, B - V]$ -plane); consequently,

$$(U - B)_0 = Q + W[(B - V)_0]. \quad (\text{A6})$$

Another important consideration, unrelated to the one just discussed, is the validity of the standard law for interstellar extinction in the context in which we are using it. Here we do not intend to discuss the chance that

TABLE B1
25 × 25 SUBSET OF 500 × 500 PIXEL RASTERS

J^*	I^*	159	160	161	162	163	164	165	166	167	168	169	170	171	172	173	174	175	176	177	178	179	180	181	182	183	
$F(U)$																											
252	498	584	510	428	341	370	401	431	379	251	210	152	143	177	168	136	171	238	233	162	114	115	108	128	140		
253	537	591	457	374	316	407	565	505	384	346	267	190	161	190	186	141	146	206	195	120	115	136	131	154	154		
254	483	471	363	311	543	534	356	558	503	178	154	184	186	148	127	159	190	143	109	113	119	143	162	162	154		
255	517	579	389	345	414	431	477	520	681	585	381	239	160	185	199	156	132	182	194	157	120	124	131	155	175		
256	584	557	403	380	415	438	415	429	554	494	381	279	208	231	211	147	110	129	149	119	105	133	131	157	158		
257	519	557	449	479	482	406	395	406	385	362	438	603	505	330	322	367	377	234	154	119	92	101	121	144	157	195	
258	499	479	449	337	341	352	400	400	511	495	471	373	371	490	529	326	204	152	105	126	129	138	152	155	187		
259	465	492	472	374	341	352	400	400	511	487	471	432	365	401	382	334	284	215	173	138	99	108	118	129	185		
260	489	533	441	369	317	380	394	394	385	536	442	462	492	429	408	379	320	308	276	248	211	152	95	114	103	141	
261	399	424	412	321	275	294	306	306	306	427	462	492	492	416	416	416	369	301	269	208	153	111	85	90	109	141	
262	406	399	348	340	377	345	373	373	436	402	454	463	378	310	354	310	278	215	160	124	102	102	120	147	193		
263	359	349	417	490	441	429	397	397	456	423	463	676	676	349	349	382	382	349	254	215	160	124	102	102	120	147	193
264	335	296	341	337	437	529	509	509	619	636	618	508	402	497	689	403	286	204	148	129	106	110	114	150	235		
265	318	303	300	299	378	518	579	535	601	602	490	384	340	377	397	336	280	211	133	118	100	124	100	128	141		
266	324	295	287	267	328	395	486	443	446	470	416	429	418	421	349	285	256	210	168	116	103	118	134	282	334		
267	299	296	273	258	306	408	436	436	432	378	461	553	494	369	272	242	204	152	122	121	116	152	227	337	337		
268	305	293	295	261	290	404	442	475	491	415	330	306	305	301	309	252	232	224	169	152	116	138	121	219	285		
269	398	402	301	282	333	410	422	402	487	388	295	270	229	221	254	228	197	206	192	197	100	151	219	249	249		
270	323	342	321	348	403	393	352	374	400	330	229	233	213	167	174	198	228	247	200	179	115	98	172	249	241		
271	301	329	367	386	447	476	368	455	596	482	334	282	296	262	178	164	214	247	249	207	164	117	119	311	330		
272	319	398	538	501	397	335	427	520	377	321	368	435	465	431	250	250	293	257	178	154	160	105	193	233	208		
273	308	434	386	553	449	449	446	446	278	279	403	853	1326	805	566	376	298	245	231	178	103	105	178	225	224		
274	287	442	557	499	560	607	343	210	218	313	418	670	739	552	427	422	341	239	192	166	116	95	168	234	251		
275	372	415	522	501	530	528	449	287	319	370	405	419	359	349	291	362	412	298	249	219	148	96	161	216	220		
276	371	467	582	540	489	518	432	374	346	382	468	364	344	278	260	283	316	335	280	250	176	114	163	213	222		
$F(B)$																											
252	537	613	603	483	400	420	468	484	394	290	260	214	211	228	207	193	227	252	213	190	173	172	201	212	212		
253	552	556	477	407	377	467	608	550	442	369	320	228	209	257	233	190	177	213	188	153	152	177	200	220	234		
254	491	499	409	377	403	460	557	530	534	379	240	215	254	265	202	167	215	228	175	152	177	177	206	234	263		
255	500	588	421	431	490	487	489	509	589	599	400	278	187	268	184	185	215	258	194	185	215	228	183	188	263		
256	583	621	468	434	478	470	457	451	524	492	409	344	257	293	267	186	169	184	257	178	154	166	146	200	231		
257	504	604	473	433	492	434	434	434	464	444	419	354	352	382	380	266	197	172	160	139	140	156	199	247			
258	603	537	541	432	429	436	412	394	482	475	408	354	352	382	380	266	197	160	127	134	166	220	212	291			
259	477	519	463	430	395	402	424	455	503	482	460	379	392	475	487	321	231	213	190	177	177	188	197	223			
260	472	544	448	406	368	411	499	516	516	458	426	366	356	366	360	349	337	321	267	198	148	139	169	176	207		
261	419	455	426	344	329	344	335	433	529	516	439	466	466	466	466	466	347	321	267	198	148	139	169	176	207		
262	418	431	391	390	406	394	417	468	405	453	495	389	422	331	305	287	285	330	309	303	265	218	189	214	239		
263	399	363	347	322	374	472	493	495	489	422	311	247	247	247	247	247	247	247	247	247	247	247	247	247	247		
264	420	417	358	387	458	446	446	446	446	416	416	389	389	389	389	389	389	389	389	389	389	389	389	389	389		
270	363	354	374	422	424	474	477	477	472	472	472	401	401	401	401	401	401	401	401	401	401	401	401	401	401		
271	345	367	377	424	450	356	367	367	367	405	336	334	334	334	334	334	334	334	334	334	334	334	334	334	334		
272	347	378	473	488	417	325	405	405	405	405	405	405	405	405	405	405	405	405	405	405	405	405	405	405	405		
273	327	437	557	493	428	357	273	273	273	273	273	273	273	273	273	273	273	273	273	273	273	273	273	273	273		
274	324	434	497	473	489	491	307	235	253	310	310	310	310	310	310	310	310	310	310	310	310	310	310	310	310		
275	373	397	469	470	511	460	395	297	319	370	366	358	358	358	358	358	358	358	358	358	358	358	358	358	358		
276	364	442	501	468	456	459	459	459	459	459	459	459	459	459	459	459	459	459	459	459	459	459	459	459	459		

TABLE B1—Continued

J^*	$\backslash I^*$	159	160	161	162	163	164	165	166	167	168	169	170	171	172	173	174	175	176	177	178	179	180	181	182	183
252	F(V)	812	940	915	812	684	755	818	859	737	560	526	476	461	518	433	410	478	508	469	395	387	433	465	516	
253		809	913	782	705	676	819	949	917	658	627	545	466	522	512	428	452	469	489	416	379	446	505	527	530	
254		752	804	679	640	722	821	883	925	873	856	720	513	471	517	557	462	427	432	466	392	386	436	489	500	557
255		816	938	730	699	812	822	932	829	948	857	732	573	449	511	545	441	421	456	491	437	406	464	509	557	578
256		809	897	729	732	794	832	807	773	821	765	717	687	534	591	540	415	388	404	404	404	404	474	550	576	601
257		758	842	776	733	757	819	788	689	753	765	722	630	643	646	550	453	381	370	344	336	399	478	551	612	620
258		737	818	810	730	741	775	706	715	774	864	841	675	661	680	672	549	454	396	359	384	436	502	528	548	595
259		742	751	749	725	688	714	732	759	805	789	780	685	707	789	646	551	475	433	404	491	505	549	560	560	575
260		756	808	740	698	655	693	732	812	790	785	775	629	688	696	669	661	587	536	438	401	431	474	463	514	575
261		667	699	681	621	604	609	722	838	764	753	839	673	665	674	665	667	625	574	460	385	360	409	465	509	559
262		624	654	649	666	717	704	735	766	695	775	888	628	586	645	727	692	635	587	495	409	352	393	433	451	505
263		606	642	656	725	781	757	754	732	735	926	1092	790	690	740	876	727	616	622	505	437	398	408	452	457	540
264		593	612	630	691	711	816	766	797	862	957	860	753	651	848	1416	804	634	547	443	446	425	433	481	538	538
265		561	584	633	633	684	818	876	820	890	944	792	640	621	672	766	697	640	538	418	417	430	401	397	561	1103
266		584	581	596	600	652	763	901	768	812	761	671	652	703	784	693	642	620	577	472	408	430	398	431	661	1202
267		547	551	565	583	615	768	783	837	766	627	642	772	782	688	623	598	531	463	411	429	433	511	610	618	
268		566	589	586	580	653	779	802	820	791	697	569	532	523	545	610	583	554	472	441	388	427	523	612	639	
269		636	652	596	610	647	736	703	653	730	643	533	491	484	492	555	532	550	475	461	374	353	469	567	579	
270		592	589	580	651	694	699	649	651	693	609	507	495	491	415	490	521	551	560	473	440	357	350	477	616	581
271		570	587	647	667	680	631	615	717	705	615	544	531	477	411	431	496	577	580	492	452	373	368	496	614	537
272		544	607	665	700	658	567	550	622	582	584	587	644	695	695	557	590	545	486	433	369	344	369	395	524	
273		528	639	738	702	673	600	498	471	464	530	597	906	1377	1177	790	620	588	514	465	443	386	359	486	578	
274		533	641	716	694	773	736	570	481	476	537	618	729	829	810	635	637	642	525	470	464	385	368	489	592	584
275		560	582	676	747	813	728	659	573	567	637	603	534	537	541	639	672	603	557	534	412	364	492	590	577	
276		569	643	723	708	688	675	632	614	635	702	599	560	547	567	589	639	635	595	621	479	345	444	577	575	

TABLE B2
25 × 25 CENTER OF 50 × 50 PIXEL COMPRESSED RASTERS

$J'' \setminus I''$	12	13	14	15	16	17	18	19	20	21	22	23	24	25	26	27	28	29	30	31	32	33	34	35	36	
$P(I)$	48	59	74	79	379	397	373	239	199	332	445	287	174	147	97	103	157	81	266	118	59	71	51	71	93	
15	56	63	81	114	443	473	324	232	585	303	264	256	189	127	131	104	232	81	62	58	48	54	54	54		
16	56	70	85	135	194	243	214	193	822	420	220	191	223	190	150	223	141	281	230	97	59	80	71	45		
17	63	92	132	540	296	126	138	139	181	210	289	171	185	266	214	272	306	167	194	126	70	67	54	54		
18	63	101	109	129	217	163	243	242	203	236	185	142	135	188	263	376	472	358	146	147	246	69	76	59		
19	101	109	300	251	201	213	238	191	286	196	218	116	126	126	169	158	272	323	164	122	133	164	99	86	70	
20	149	235	164	304	220	200	216	408	201	251	273	217	177	135	124	132	191	298	337	330	87	168	581	189	83	
21	118	129	218	180	286	408	233	228	311	498	273	227	165	265	288	385	447	103	204	131	136	74	98	98	98	
22	115	155	238	201	311	226	196	323	360	293	346	647	288	385	219	233	123	190	219	288	428	219	112	96	86	
23	388	145	261	253	145	170	154	175	578	899	326	317	753	606	265	230	305	275	198	186	204	565	556	132	104	160
24	148	154	239	181	198	661	643	191	211	230	347	327	384	391	400	312	304	235	181	207	223	147	109	154	154	
25	163	97	90	102	119	190	449	194	197	127	185	235	174	265	372	257	238	570	598	615	485	250	194	200	177	
26	141	152	150	189	395	401	182	196	203	306	398	1041	1666	369	240	190	661	343	228	180	108	114	114	114	114	
27	118	129	218	180	286	408	233	228	311	498	273	227	165	265	288	385	447	223	278	240	217	152	246	456	202	
28	115	155	238	201	311	226	196	323	360	293	346	647	288	385	219	233	123	190	219	288	428	219	112	96	86	
29	101	118	136	165	227	570	311	227	165	156	218	293	444	261	336	302	274	283	753	347	248	211	219	219	219	
30	95	107	126	120	150	410	496	198	230	230	347	324	264	328	276	298	286	298	714	536	225	224	264	197	197	
31	85	97	90	102	119	190	449	194	197	127	185	235	174	265	372	257	238	570	598	615	485	250	194	200	177	
32	72	66	88	108	131	239	245	206	151	151	151	151	151	151	151	153	303	219	196	377	590	936	706	303		
33	81	82	96	98	91	114	174	239	206	151	149	168	130	203	324	238	271	304	338	401	364	326	280	258	150	
34	71	75	74	90	84	133	159	208	530	224	182	178	165	162	519	471	266	306	334	291	236	268	251	507	441	
35	192	55	80	123	80	88	139	187	192	298	356	297	345	179	160	163	243	272	356	363	477	194	153	197	197	
36	63	65	69	94	142	122	77	131	160	153	275	400	292	278	232	189	173	147	279	138	131	130	111	99	81	
37	79	76	72	94	100	87	271	324	119	139	224	325	290	161	264	120	113	115	129	93	139	65	65	53	53	
38	86	215	91	76	112	87	147	172	94	90	119	143	146	164	102	102	102	102	102	93	102	78	56	56	56	
39	94	78	100	108	73	160	71	112	104	108	91	96	114	135	110	118	103	98	80	96	102	71	67	54	54	
	12	13	14	15	16	17	18	19	20	21	22	23	24	25	26	27	28	29	30	31	32	33	34	35	36	

TABLE B2—Continued

$J'' \setminus I''$	12	13	14	15	16	17	18	19	20	21	22	23	24	25	26	27	28	29	30	31	32	33	34	35	36	
15	122	146	174	193	356	414	324	309	409	464	358	278	268	198	194	272	159	276	169	112	119	93	101	121		
16	138	163	201	252	442	466	397	354	343	609	381	357	327	290	236	225	278	196	298	258	164	130	100	91	97	
17	148	185	216	252	321	367	308	331	339	688	460	358	323	335	295	249	281	231	287	264	166	122	136	133	95	
18	172	225	260	509	396	296	336	349	430	446	372	323	379	447	417	328	325	338	255	270	202	139	126	105	101	
19	238	243	275	368	335	436	509	471	477	421	375	327	325	381	419	479	490	393	252	246	279	211	138	137	111	
20	327	637	430	418	409	467	452	487	433	421	332	344	346	392	346	458	503	392	284	237	222	235	182	148	126	
21	346	346	481	437	417	447	595	412	559	504	441	410	374	361	359	389	474	492	425	211	251	441	251	159	142	
22	314	379	492	394	418	396	526	626	631	668	711	532	635	406	425	416	512	478	455	239	239	288	221	207	161	175
23	1249	326	417	416	487	680	990	712	814	1005	876	708	622	563	479	375	489	515	479	474	314	224	190	184	197	
24	330	327	333	336	361	604	609	647	838	996	855	961	919	755	667	602	525	515	466	597	561	268	197	231	236	
25	316	357	296	319	319	499	582	784	1093	1257	1379	1257	1266	1298	876	704	608	527	540	512	541	373	226	206	241	
26	280	264	293	350	626	744	484	610	672	789	1222	1852	3619	4034	1297	704	608	589	523	645	523	378	284	227	229	
27	246	248	336	337	510	712	553	597	600	680	1013	1938	5758	1595	820	787	652	605	435	519	546	312	245	252	252	
28	236	263	328	339	483	691	559	580	596	594	793	1367	1974	1596	1390	1029	954	789	625	574	477	584	408	316	338	
29	210	225	242	298	372	695	611	574	478	484	625	836	1112	933	936	1134	1000	783	920	677	823	444	381	371	412	
30	196	202	222	240	289	550	669	485	477	419	532	634	712	812	856	775	801	838	789	891	661	361	404	464	413	
31	172	178	183	212	259	372	580	439	484	391	454	498	474	555	659	615	621	775	678	580	417	402	418	372	372	
32	157	148	177	211	224	296	425	452	467	421	390	364	402	599	479	480	523	635	849	867	728	531	552	469	295	
33	159	160	170	186	213	275	349	440	427	389	426	431	350	423	533	467	582	597	596	624	615	577	469	389	266	
34	162	137	155	168	179	267	301	396	579	447	428	425	447	383	370	1020	611	515	616	576	500	483	395	1023	892	
35	434	134	159	193	163	182	246	340	373	460	493	497	524	385	364	362	443	513	513	997	503	493	304	273	299	
36	150	149	155	211	186	157	209	262	300	422	522	470	417	408	365	349	322	376	306	286	251	227	209	190	188	
37	170	169	160	186	174	162	283	319	231	271	345	433	416	311	343	261	277	265	210	230	164	169	145	136	136	
38	170	446	180	166	180	188	204	219	186	199	238	277	283	310	393	236	277	195	205	189	184	180	146	140	140	
39	169	169	190	207	168	317	155	175	193	188	311	201	223	244	260	246	245	218	207	184	175	165	156	153	132	

significant differences may exist between the mean properties of interstellar dust in the solar neighborhood and in the inner region of M83, but merely wish to point out that the solar neighborhood law of interstellar extinction lumps together the effects of scattering and absorption, which is not appropriate when considering the effects of internal extinction on the integrated light of an object such as M83, since light scattered out of a particular line of sight by dust will be replaced by light scattered into the line of sight from other directions within the object. Clearly, the relationship between these two quantities will vary in a complicated way, depending on the geometry of the object, including the distribution of the dust within it, and on the scattering phase function of the dust. In any case, the ratio of the *effective* amount of light scattered out of the line of sight to the amount of light *absorbed* by the dust is likely to be much different than in an observation of a single star within our galaxy. Therefore, if the ratio ($\sigma_{\text{scat}}/\sigma_{\text{ext}}$) for the dust, i.e., its albedo, is significantly wavelength dependent, the same dust will yield different reddening laws in the two cases. The wavelength dependence in the visible of the albedo of interstellar dust in the galaxy is not well known, but available estimates based on measurements of the diffuse galactic light (van de Hulst and de Jong 1969) and on the properties of grain models constructed to fit the extinction and polarization measurements (Greenberg 1968) suggest that there is unlikely to be a significant wavelength dependence of the albedo within the range of the U , B , and V passbands.

APPENDIX B TABULAR SURFACE BRIGHTNESS DATA

The original UBV intensity data files of 1000×1000 pixels were compressed by factors of 2 in each direction (called C2) and by factors of 20 (C20). In C2 ($I', J'; I', J' = 1,500$), the pixel (I', J') consists of the intensity average of the four original pixels $I = 2*(I' - 1) + 1$ to $2*(I' - 1) + 2$ and $J = 2*(J' - 1) + 1$ to $2*(J' - 1) + 2$. For C20 the corresponding formulae for (I'', J'') are $I = 20*(I'' - 1) + 1$ to $20*(I'' - 1) + 20$, etc.

The tables show one set of 25×25 pixels from C2 and one set of 25×25 pixels from C20. The tables give coordinates I' , J' , I'' , and J'' . The pixel sizes are $1''.488$ and $14''.88$ square in C2 and C20, so that for C2

$$m = 27.5 - 5 \log(1.488) - 2.5 \log F = 26.64 - 2.5 \log F, \quad (B1)$$

and for C20

$$m = 21.64 - 2.5 \log F.$$

Only UBV are given in the tables.

REFERENCES

- Alcaino, G. 1974, *Astr. Ap. Suppl.*, **13**, 305.
 Allen, C. W. 1973, *Astrophysical Quantities* (London: Athlone Press), p. 202.
 Bash, F. N., Green, E., and Peters, W. L. III. 1977, *Ap. J.*, **217**, 464.
 Chiu, L.-T. G. 1976, *Pub. A.S.P.*, **88**, 803.
 Danver, C.-G. 1942, *Ann. Obs. Lund*, No. 10.
 Davis, J. C., Jr., Talbot, R. J., Jr., and Jensen, E. B. 1978, *Bull. AAS*, **10**, 423.
 de Vaucouleurs, G. 1961, *Ap. J. Suppl.*, **5**, 233.
 de Vaucouleurs, G., de Vaucouleurs, A., and Corwin, H. G., Jr. 1976, *Second Reference Catalogue of Bright Galaxies* (Austin: University of Texas Press) (RC2).
 Dixon, M. E. 1971, *Ap. J.*, **164**, 411.
 Dixon, M. E., Ford, V. L., and Robertson, J. W. 1972, *Ap. J.*, **174**, 17.
 Evans, D. S. 1956, in *Vistas in Astronomy*, 2, ed. A. Beer (London: Pergamon), p. 1555.
 Freeman, K. C. 1970, *Ap. J.*, **160**, 811.
 Fujimoto, M. 1968, *IAU Symposium No. 29, Nonstable Phenomena in Galaxies*, ed. M. Arakelian (Yerevan: Armenian Academy of Sciences), p. 453.
 Gallagher, J. 1978, private communication.
 Greenberg, J. M. 1968, in *Nebulae and Interstellar Matter*, ed. B. M. Middlehurst and L. H. Aller (Chicago: University of Chicago Press), chap. 6.
 Jensen, E. B. 1977, Ph.D. thesis, The University of Arizona.
 Johnson, H. L. 1963, in *Basic Astronomical Data*, ed. K. Aa. Strand (Chicago: University of Chicago Press), chap. 11.
 Kormendy, J. 1977a, *Ap. J.*, **214**, 359.
 —. 1977b, *Ap. J.*, **217**, 406.
 Kunkel, W. E. 1976, unpublished.
 Landolt, A. U. 1973, *A.J.*, **78**, 959.
 Larson, R. B. 1977, in *The Evolution of Galaxies and Stellar Populations*, ed. B. M. Tinsley and R. B. Larson (New Haven: Yale University Press), pp. 108–112.
 Lin, C. C., and Shu, F. H. 1964, *Ap. J.*, **140**, 646.
 Lynds, B. T. 1970, in *IAU Symposium No. 38, The Spiral Structure of Our Galaxy*, ed. W. Becker and G. Contopoulos (Dordrecht: Reidel), p. 26.
 —. 1972, in *IAU Symposium No. 44, External Galaxies and Quasi-stellar Objects*, ed. D. S. Evans (Dordrecht: Reidel).
 —. 1974, *Ap. J. Suppl.*, **28**, 391.
 Pettit, E. 1954, *Ap. J.*, **120**, 413.
 Racine, R. 1973, *A.J.*, **78**, 180.
 Roberts, W. W. 1969, *Ap. J.*, **158**, 123.
 Rogstad, D. H., Lockhart, I. A., and Wright, M. C. H. 1974, *Ap. J.*, **193**, 309.
 Rots, A. H. 1975, *Astr. Ap.*, **45**, 43.
 Sandage, A. 1961, *The Hubble Atlas of Galaxies* (Washington: Carnegie Institution of Washington).
 Schweizer, F. 1975, in *Proc. CNRS International Colloquium, La Dynamique Des Galaxies Spirals*, ed. L. Welischew (Paris: Centre National de la Recherche Scientifique), p. 339.
 —. 1976, *Ap. J. Suppl.*, **31**, 313.
 Searle, L., Sargent, W. L. W., and Bagnuolo, W. G. 1973, *Ap. J.*, **179**, 427.
 Strom, K. M., Strom, S. E., Jensen, E. B., Moller, J., Thompson, L. A., and Thuan, T. X. 1977, *Ap. J.*, **212**, 335.
 Tinsley, B. M. 1968, *Ap. J.*, **151**, 547.
 Toomre, A. 1977, *Ann. Rev. Astr. Ap.*, **15**, 437.
 Tsubaki, T., and Engvold, O. 1975, *AAS Photo-Bulletin*, **9**, 17.
 van de Hulst, H. C., and de Jong, T. 1969, *Physica*, **41**, 151.
 Visser, H. C. D. 1978, Ph.D. thesis, Groningen University.
 Wielen, R. 1976, preprint.
 Wells, D. 1975, *KPNO and CTIO Quart. Bull.* July–Sept., p. 12.
 Westerlund, B. E., and Wall, J. V. 1969, *A.J.*, **74**, 335.
 Woodward, P. R. 1976, *Ap. J.*, **207**, 484.
 Yuan, C. 1969, *Ap. J.*, **158**, 889.
 —. 1977, in *The Evolution of Galaxies and Stellar Populations*, ed. B. M. Tinsley and R. B. Larson (New Haven: Yale University Press), pp. 126–127.

REGINALD J. DUFOUR, ERIC B. JENSEN, and RAYMOND J. TALBOT, JR.: Department of Space Physics and Astronomy, Rice University, Houston, TX 77001

PLATE 3

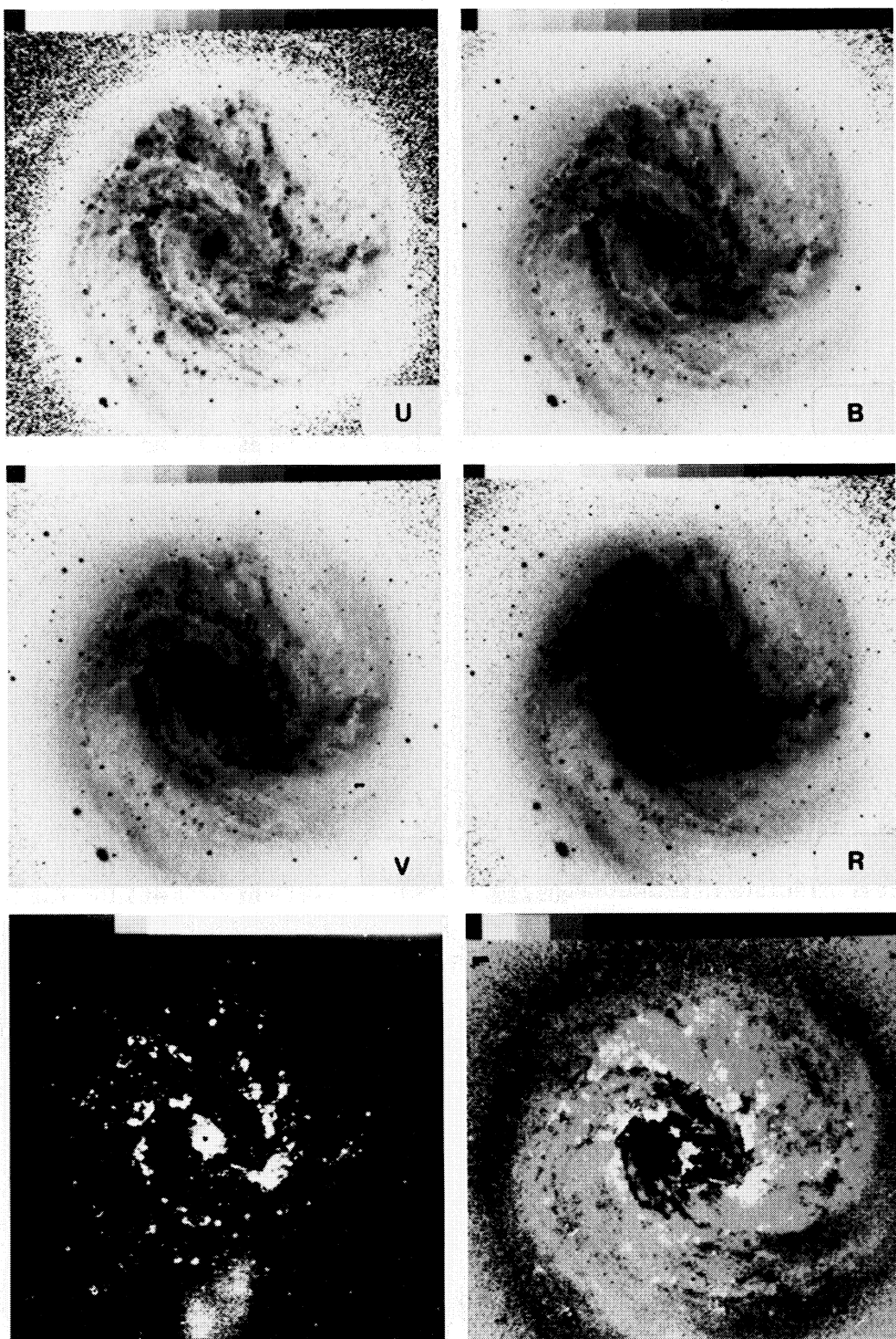


FIG. 1.—Calibrated, sky-subtracted magnitude maps for U , B , V , R , and $H\alpha$; these are 500×500 displays of data compressed 2×2 . In each wedge the rightmost whole step is $18.0 \text{ mag arcsec}^{-2}$ and the steps are 0.5 mag . Fig. 1f(lower right) is a composite of the $H\alpha$ map and a $(B - V)$ map with only pixels redder than 0.9 retained. This map emphasizes the intimate relationship between dust lanes and H II regions in M83. North is at the top, east is on the left. The pictures are $744''$ wide.

TALBOT *et al.* (see page 96)

PLATE 4

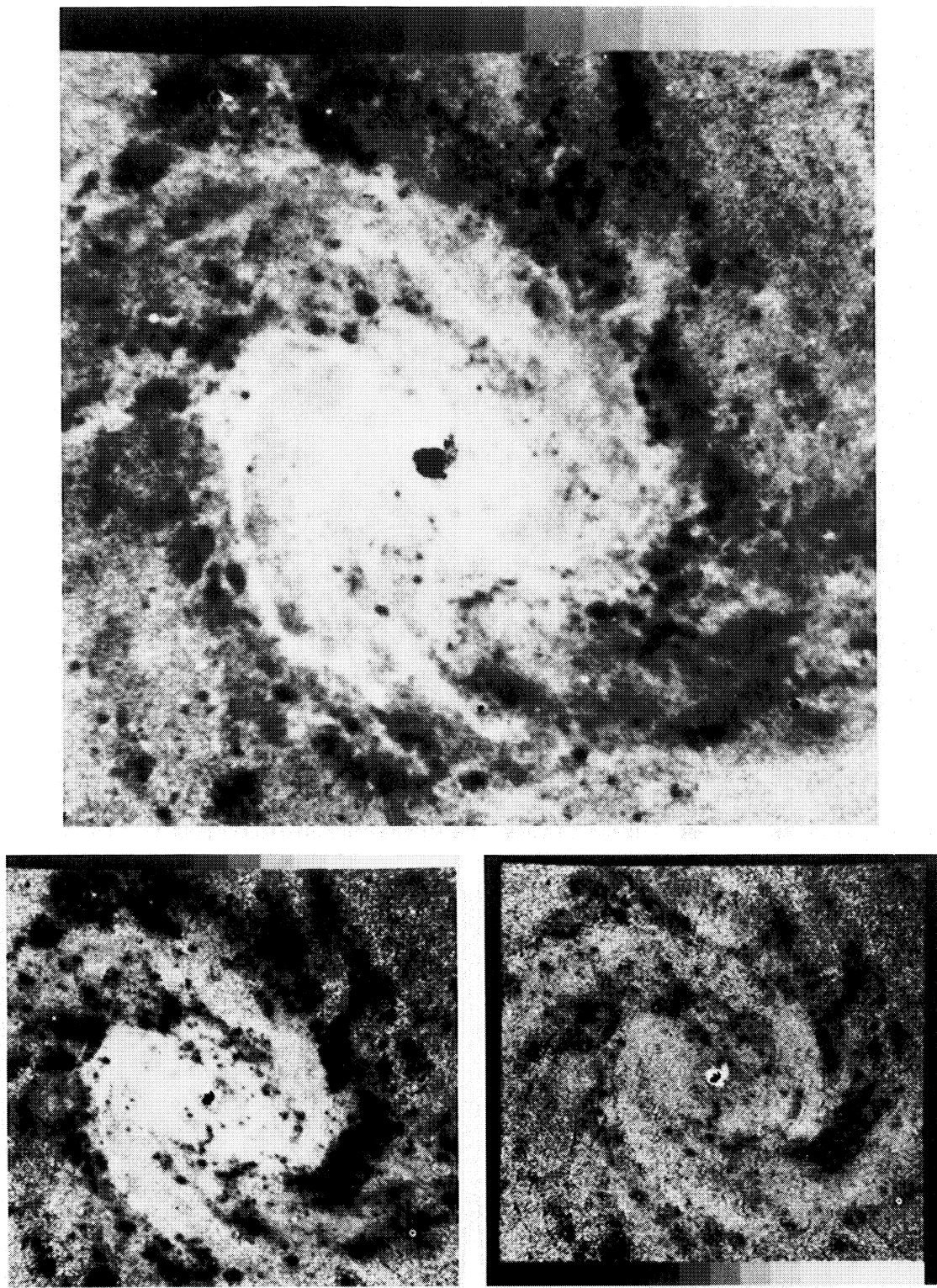


FIG. 2.—Calibrated, sky-subtracted color maps for $B - V$ (top), $U - B$ (lower left), and Q (lower right). These are the center 512×512 pixels of the original 1000×1000 rasters. The rightmost whole step is $B - V = 1.1$, $U - B = 0.7$, and $Q = 0.3$. The steps are 0.1 mag in each case.

TALBOT *et al.* (see page 96)